

Geochemistry, Geophysics, Geosystems

RESEARCH ARTICLE

10.1029/2020GC009547

Key Points:

- The seismic strain rate ranges 10^{-18} to 10^{-15} s^{-1} with a local minimum or neutral bending plane at 15 km depth within the Hawaiian lithosphere
- The seismic strain rate and flexure are best-reproduced by viscoelastic loading models with frictional coefficient $\mu_f = 0.3 \pm 0.1$
- Rapid reduction in seismic strain rate and observations of seismic P axes suggest a lateral reduction in μ_f approaching central Island of Hawaii

Supporting Information:

Supporting Information may be found in the online version of this article.

Correspondence to:

A. Bellas,
ashley.bellas@colorado.edu

Citation:

Bellas, A., & Zhong, S. J. (2021). Seismic strain rate and flexure at the Hawaiian Islands constrain the frictional coefficient. *Geochemistry, Geophysics, Geosystems*, 22, e2020GC009547. <https://doi.org/10.1029/2020GC009547>

Received 16 NOV 2020

Accepted 23 FEB 2021

Author Contributions:

Conceptualization: S. J. Zhong

Data curation: A. Bellas

Formal analysis: A. Bellas

Funding acquisition: S. J. Zhong

Investigation: A. Bellas

Methodology: A. Bellas, S. J. Zhong

Project Administration: S. J. Zhong

Software: A. Bellas, S. J. Zhong

Supervision: S. J. Zhong

Validation: S. J. Zhong

Visualization: A. Bellas, S. J. Zhong

Writing – original draft: A. Bellas, S. J. Zhong

Writing – review & editing: A. Bellas

Seismic Strain Rate and Flexure at the Hawaiian Islands Constrain the Frictional Coefficient

A. Bellas¹  and S. J. Zhong¹ 

¹Department of Physics, University of Colorado, Boulder, CO, USA

Abstract Flexure occurs on intermediate geologic timescales (~ 1 Myr) due to volcanic-island building at the Island of Hawaii, and the deformational response of the lithosphere is simultaneously elastic, plastic, and ductile. At shallow depths and low temperatures, elastic deformation transitions to frictional failure on faults where stresses exceed a threshold value, and this complex rheology controls the rate of deformation manifested by earthquakes. In this study, we estimate the seismic strain rate based on earthquakes recorded between 1960 and 2019 at Hawaii, and the estimated strain rate with 10^{-18} – 10^{-15} s^{-1} in magnitude exhibits a local minimum or neutral bending plane at 15 km depth within the lithosphere. In comparison, flexure and internal deformation of the lithosphere are modeled in 3D viscoelastic loading models where deformation at shallow depths is accommodated by frictional sliding on faults and limited by the frictional coefficient (μ_f), and at larger depths by low-temperature plasticity and high-temperature creep. Observations of flexure and the seismic strain rate are best-reproduced by models with $\mu_f = 0.3 \pm 0.1$ and modified laboratory-derived low-temperature plasticity. Results also suggest strong lateral variations in the frictional strength of faults beneath Hawaii. Our models predict a radial pattern of compressive stress axes relative to central Hawaii consistent with observations of earthquake pressure (P) axes. We demonstrate that the dip angle of this radial axis is essential to discerning a change in the curvature of flexure, and therefore has implications for constraining lateral variations in lithospheric strength.

1. Introduction

Deformation of the Earth in response to forcing transitions from elastic to viscous is increasing with timescale and temperature. For example, on the short timescales relevant to forcing from seismic waves and tides (seconds to days), the deformational response of the mantle is essentially elastic. Meanwhile, the solid rocks in the mantle are also warm, weak, and deform viscously in response to forcing imposed on very long geologic timescales ($>10^6$ – 10^9 years) by temperature gradients between the surface and the core-mantle boundary. In contrast, the surface thermal boundary layer (or lithosphere) is cold, very stiff, and typically behaves like an elastic plate even on the long timescales relevant to mantle convection. However, lithospheric rocks are also capable of viscous flow where they are warmed and subject to forcing on long timescales (e.g., continental rifting, magmatism, lithospheric small-scale convection). On intermediate timescales (10^3 – 10^6 years), both modes of deformation are relevant to the dynamics of mantle-lithosphere systems, and such processes are fundamentally viscoelastic (e.g., subduction zone dynamics, glacial isostatic adjustment, flexure, isostasy, orogeny, and tectonics). Since such processes collectively are the manifestation of plate tectonics, it is essential to improve and expand our understanding of viscoelastic rheology in the mantle and lithosphere. In particular, the volcanic Island of Hawaii has been steadily built over the past ~ 1 Myr and acts as a surface load which induces viscoelastic deformation and flexure. Observations of this deformational response to loading offer a unique opportunity to constrain the rheology of the intraplate lithosphere at the Island of Hawaii.

The elastic properties of the crust and mantle lithosphere have been estimated by surface wave seismic tomography (e.g., Ritzwoller et al., 2004), and mineral physics experiments (e.g., Christensen, 1966) in terms of the shear modulus, $\mu = 3 \times 10^{10}$ – 7×10^{10} Pa. Mineral physics experiments also show that the lithosphere deforms permanently under three distinct mechanisms: (i) brittle failure also known as frictional sliding at low pressures and temperatures ($< \sim 400^\circ\text{C}$), (ii) low-temperature plasticity also known as dislocation glide or Peierls creep at intermediate pressures and temperatures (~ 400 – 800°C), and (iii) high-temperature creep also known as dislocation and/or diffusion creep at high pressures and temperatures ($> \sim 800^\circ\text{C}$). Of

the three, high-temperature creep is generally well-understood thanks to laboratory experiments (Hirth & Kohlstedt, 2003), post-seismic deformation studies (Freed et al., 2010; Hu & Wang, 2012), and glacial isostatic adjustment (Mitrovica & Forte, 1997). However, low-temperature plasticity and frictional sliding are less established in comparison.

For example, a long history of mineral physics studies report different parameter values and strengths of low-temperature plasticity at lithospheric conditions (e.g., Goetze & Evans, 1979; Idrissi et al., 2016; Katayama & Karato, 2008; Mei et al., 2010; Raterron et al., 2004), and although recent progress in understanding grain-size- and length-scale-dependence has helped to reconcile these differences (Kumamoto et al., 2017), the laboratory flow laws still overestimate the effective elastic thickness of oceanic lithosphere by a factor of ~ 2 (Bellás et al., 2020). In addition, low-temperature plasticity may be so strongly sensitive to strain-induced back-stress in the lattice structure that it is completely phased out after 2% strain accumulation occurs in lithospheric materials (Hansen et al., 2019). Finally, some studies show that dislocation-glide is not possible in rocks subjected to hydrous-alteration and serpentinization (Hansen et al., 2020), while others show evidence of distributed dislocation glide and frictional sliding in a complex deformation mechanism known as the semi-brittle regime (Chernak & Hirth, 2010). Collectively, these studies suggest that low-temperature plasticity is sensitive to composition and tectonic setting, leaving much to be learned about its control on lithospheric dynamics.

An equally complicated history is presented in the literature on frictional sliding. For example, laboratory studies estimate the frictional coefficient is largely insensitive to temperature and rock type but decreases with increasing normal stress, such that $\mu_f = 0.85$ for $\sigma_n < 200$ MPa, $\mu_f = 0.6$ for $\sigma_n > 200$ MPa (Byerlee, 1978), and $\mu_f = 0.5$ for $\sigma_n \sim 300$ MPa (Boettcher et al., 2007). Such laboratory estimates are approximately consistent with in situ borehole measurements at shallow depths in continental intraplate settings which require $\mu_f \sim 0.6$ (Zoback & Townend, 2001). However, geodynamic models of mantle convection require $\mu_f < 0.1$ globally for plate tectonics to emerge (e.g., Moresi & Solomatov, 1998), consistent with observations of surface heat flow at mature plate margins which require $\mu_f < \sim 0.1$ (England, 2018; Gao & Wang, 2014). Meanwhile, analysis of the dip angle of newly formed normal faults in the outer-rise region of subduction zones and at mid-ocean spreading ridges suggests $\mu_f < 0.3$ (Craig, Copley, & Middleton, 2014; Thatcher & Hill, 1995), and analysis of transform faults, specifically fracture zones between offset oceanic spreading ridges, suggests $\mu_f < 0.1$ (Behn et al., 2002). In plate interior settings like Hawaii, models of flexure and the depth distribution of seismicity suggest that $\mu_f \geq 0.25$ (Zhong & Watts, 2013). Fault strength may be sensitive to chemical alteration [e.g., serpentinization may reduce the frictional strength to $\mu_f = 0.35$ (Escartín et al., 1997)], and mechanical alteration (Collettini, 2011). Similar to low-temperature plasticity, frictional sliding appears sensitive to composition and tectonic setting.

That significant variations in μ_f exist between different tectonic settings is fundamental to the theory of plate tectonics, and it will be necessary to map the frictional strength of the lithosphere and identify the causes of variations to make progress in understanding deformation of the Earth under a unified theory. Recent studies support a first-order control of fault motion on the tectonic style of terrestrial bodies (e.g., Venus compared to Earth; Karato & Barbot, 2018), and classic observations in the Indian ocean lithosphere suggest that the tectonic style of Earth may be more complicated than “strong plates with weak boundaries” (Bull & Scrutton, 1990). The broad range of observations, processes and apparently different strengths in the frictional regime raise some important questions. For example: is the extrapolation of strength under laboratory conditions to lithospheric conditions viable? Are the apparent disagreements on the strength of faults due to differences in the methods used? Can such differences be reconciled by weakening processes? Can we discriminate between weakening by chemical and mechanical alteration, and would it explain the different tectonic styles of the solar system bodies? Finally, what is the nature of the frictional strength of the Hawaiian lithosphere, and how does it relate to other tectonic settings on Earth?

To contribute a response to such questions, we combine results from mineral physics experiments, field observations of the Hawaiian flexure system, and numerical modeling of load-induced lithospheric deformation at Hawaii to place constraints on lithospheric rheology. We estimate the seismic strain rate from earthquakes recorded over 60 years at Hawaii (1960–2019) and use it as a new constraint on frictional sliding. We formulate 3D Cartesian viscoelastic loading models including deformation from frictional sliding, low-temperature plasticity, and high-temperature creep to predict the deformational response of the

lithosphere to Hawaiian Island building. We compare numerical predictions of the principal stress axes to the seismically observed pressure (P) and tension (T) axes, discuss implications for a broken lithosphere as suggested by a recent seismic study (Klein, 2016), and compare with the observed flexure and the seismic strain rate to constrain the value of the frictional coefficient in Hawaiian lithosphere.

Observations of flexure and seismicity at Hawaii have been previously used in 3D viscoelastic loading models to constrain the rheology of frictional sliding and low-temperature plasticity (Bellas et al., 2020; Zhong & Watts, 2013). Here, we build on these studies by introducing the seismic strain rate, a new and more robust observational data set which will improve previous constraints on frictional sliding and low-temperature plasticity. In particular, flexure of the lithosphere is predominantly controlled by frictional sliding and low-temperature plasticity, such that there is trade-off between them. In previous work, the trade-off was constrained to a subset of the possible combinations based on the depth of minimum seismicity (i.e., the neutral plane in the lithosphere). Many combinations of frictional sliding and low-temperature plasticity reproduced flexure, but only a subset of models with $\mu_f = 0.25\text{--}0.7$ also reproduced the depth of the neutral plane of minimum seismicity. However, seismicity does not account for the magnitude of seismic events which may significantly perturb the depth of the inferred neutral plane. The key advancement of the present study is to take the magnitude of seismic events into account by inferring the seismic strain rate and using it in combination with flexure to constrain both frictional sliding and low-temperature plasticity more precisely. The seismic strain rate has been previously estimated for continental (England & Molnar, 1997; Holt et al., 1995; Jackson & McKenzie, 1988; Masson et al., 2005), oceanic (Gordon, 2000; Wiens & Stein, 1983) and subducted lithospheres (Billen, 2020), but the present study represents the first to investigate an oceanic region with a large number of earthquakes and significant lithospheric deformation. In the following Section 2, we present observations of flexure and infer the seismic strain rate. In Section 3, we present the numerical viscoelastic loading model, and in Section 4, the model predictions and observations are compared to constrain the value of the frictional coefficient. A Discussion of the results and Conclusions are presented in Sections 5 and 6, respectively.

2. Observations of Flexure, Stress, and the Seismic Strain Rate

We use three different observations at Hawaii to constrain lithospheric rheology in this study: lithospheric flexure, seismically derived stress, and the seismic strain rate. The flexure is recorded by three seismic reflection profiles between Kauai, Oahu and Molokai which were collected by the R/V Conrad cruise C2308 (Watts & ten Brink, 1989). We also use seismic reflection data from other seismic surveys around Hawaii (Shor & Pollard, 1964; Zucca et al., 1982). The surface of the Pacific crust is deflected by up to 5 km around Hawaii and is spread laterally over ~ 200 km between the maximum depression and the outer-rise (Section 4; Zhong & Watts, 2013). The observed flexure of the Pacific plate at Hawaii has been used previously in studies of elastic thickness (Watts & ten Brink, 1989; Wessel, 1993) and lithospheric rheology (Bellas et al., 2020; Zhong & Watts, 2013).

The second observation is the orientation of stresses at the Island of Hawaii based on seismic observations of the P and T axes, which approximate the directions of maximum compression and extension, respectively. Klein (2016) demonstrates that many events below the neutral plane of the bending lithosphere produce radial P axes which point toward a stress center located between Mauna Kea and Mauna Loa (presented in detail later). A gap in seismicity indicates the neutral plane is located at 21 km below sea level (Klein, 2016), as does a transition from radial extensional stress at shallow depths <20 km to radial compression at depths >25 km relative to central Hawaii (Ross et al., 2007). Klein also argues that the lithosphere at Hawaii is broken based on (i) observations of a low seismicity zone with ~ 30 km radius centered on Hawaii and (ii) comparison of radial P axes with principal stresses in a 2D cantilever beam model that is loaded at one end. Klein demonstrated good agreement between the observed radial P axes and stresses in a 2D cantilever beam that is loaded at one end, which indicated uniformly concave downward curvature in the Hawaiian lithosphere. In his study, that the lithosphere is broken refers to a proposed region of negligible flexural strength beneath central Hawaii which may explain why stresses in the Hawaiian lithosphere appeared similar to those in a cantilever beam loaded at one end. The “weak hole” has ~ 30 km radius and persists through the seismogenic layer based on low seismicity and may also persist to even larger depths based on the inferred uniformly concave-downward curvature. However, the inferred curvature is dependent on the

Table 1
Seismic Data Distribution

Magnitude type	Number	Average magnitude	Max magnitude	Standard deviation
Raw data				
m_L	17,605	2.8	6.1	0.32
m_D	778	3.1	4.9	0.58
m_B	262	4.4	5.8	0.42
m_W	19	5.5	7.7	0.71
m_S	5	5.4	6.1	0.41
All	18,669	2.9	7.7	0.39
After corrections				
m_L	1,246	3.1	6.1	0.57
m_D	414	3.2	4.9	0.61
m_B	203	4.3	5.6	0.41
m_W	13	5.5	6.7	0.73
m_S	4	5.4	6.1	0.47
All	1,880	3.3	6.7	0.70

Note. The applied corrections include removing events associated with magmatism, magmatism induced flank displacements, slip on the detachment plane between the pristine Pacific crust and the volcanic pile, correcting depth to be measured relative to the local surface of the deflected lithosphere, and removing events within the volcanic pile.

2D cantilever beam model, and Klein acknowledges the need to compare the observed radial P axes with principal stresses from 3D models of flexure which we present in Sections 4.2 and 5.2.

The third observational constraint used in this study is the seismic strain rate. Seismic events occurring over the past 60 years have been recorded in the ANSS catalog ComCat which is hosted by the USGS and comprises 18,669 location-magnitude data pairs in the Hawaiian region (Young et al., 1996, Table 1). We apply two corrections to the data before computing the seismic strain rate associated with flexure of the lithosphere. First, we discard 13 large events with characteristic flank-displacement focal mechanisms: magnitude ≥ 5.0 , thrust focal mechanism on a fault plane with shallow-dip, and hypocenter located in a known mobile volcano flank. Events of this nature may be associated with magma injection in the east-Kilauea rift zone which drives seaward motion of the southern flank, or with slip on the decollement surface between the volcanic load and the pristine Pacific seafloor, such as the historic 1975 Kalapana $m_W = 7.7$ event (Swanson et al., 1976). Second, the raw depth-location from the ANSS ComCat is measured relative to the local geoid, so we correct it for sea-level (5 km uniformly) and local deflection of the seafloor that best reproduces seismic reflection data (up to 5 km and spatially dependent; Section 4.1). The residual depth represents distance to the upper surface of the flexed Pacific crust. Events with residual depth less than zero are located in the volcanic pile and discarded leaving 1880 corrected events (Table 1). The seismic strain rate estimated from the depth- and event-corrected data is therefore representative of the long-term lithospheric strain rate from flexure, barring a strong influence from the following sources of error.

We do not identify or remove smaller flank- or decollement-displacement events but this should not significantly impact the results because small magnitude events contribute very little to the seismic strain rate, and

these events should be removed by the depth-correction. Only seismic events associated with earthquakes are considered, and volcanic eruptions are identified in ComCat, but we are not able to identify or remove events associated with deep magmatism. Finally, two potential caveats associated with computing seismic strain rate should be acknowledged: (i) deformation may occur aseismically, and (ii) seismic activity in the past 60 years may not be necessarily representative of the long-term average. Both of these potential caveats have been discussed thoroughly in previous studies and are generally regarded as routine and/or manageable (e.g., Masson et al., 2005). We cannot quantify the proportion of aseismic deformation as in previous studies (e.g., Masson et al., 2005) due to a lack of geodetic data to constrain the total (seismic and aseismic) strain rate for the oceanic setting of interest here. However, we compute a simplified estimate of total strain rate at Hawaii, and we can rule out significant contamination from aseismic deformation if the maximum seismic strain rate is approximately equal to this estimate. Based on 5 km of vertical deflection spread laterally over 200 km and accumulated over 1 Myr, the simplified estimate of strain rate at Hawaii $\dot{\epsilon} = 5 \times 10^3 \text{ [m]} / (200 \times 10^3 \text{ [m]} \times 10^6 \text{ [year]}) \sim 8 \times 10^{-16} \text{ s}^{-1}$ (to be referenced later). The 1 Myr age estimate for Hawaii is based on rock-dating and terraced coral reefs which also suggest that the deflection has increased linearly at least over the last 500 kyr (Moore & Clague, 1992; Zhong & Watts, 2013). Finally, we suggest that a 60-year record of seismic activity is likely to represent the long-term average because the maximum magnitude of flexural earthquakes at Hawaii is relatively small (Table 1), which suggests relatively small recurrence timescales.

The seismic strain rate is given by (Kostrov, 1974; Masson et al., 2005)

$$\dot{\epsilon}_S = \frac{1}{2\mu V \tau} \sum_{i=1}^N M_0^{(i)} \quad (1)$$

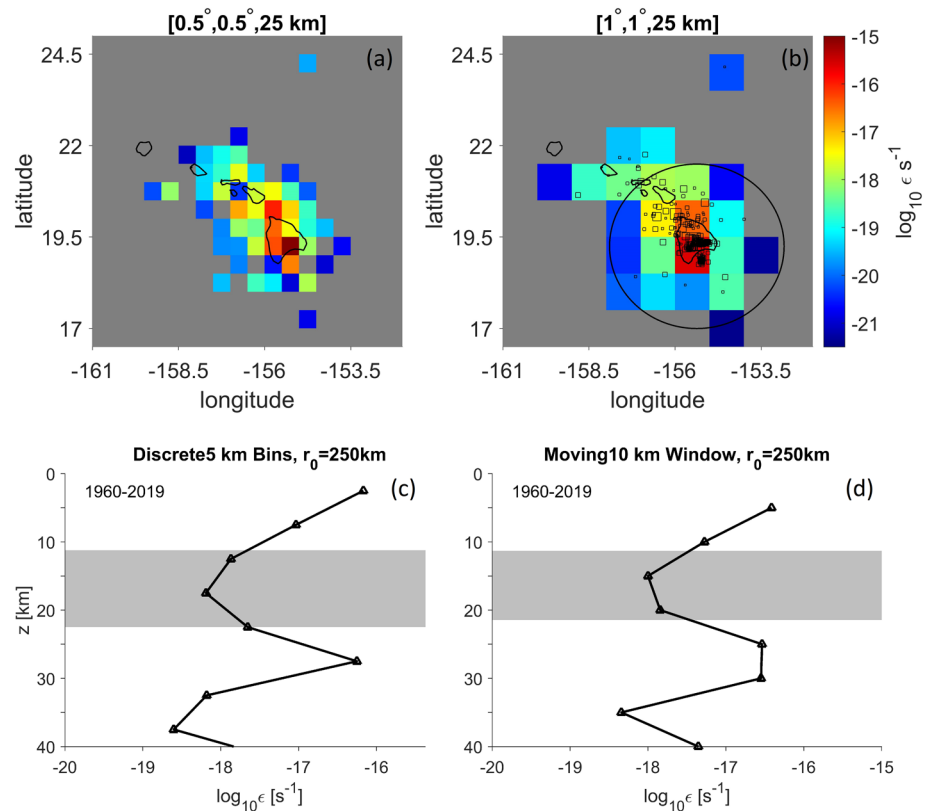


Figure 1. The seismic strain rate. The seismic strain rate in map-view at the Hawaiian Islands based on seismic data recorded over 60 years (1960–2019), in the upper 25 km and in areal bins $0.5^\circ \times 0.5^\circ$ (a), and $1.0^\circ \times 1.0^\circ$ (b) in latitude and longitude. Superposed squares in (b) represent earthquakes with magnitude ≥ 4.0 . The 1D vertical profile of seismic strain rate is averaged horizontally within a 250 km radius centered on Hawaii, and (c) vertically in discrete 5 km bins, or (d) in 10 km vertical moving windows. The depth of the neutral plane where minimal deformation occurs is located at 17.5 and 15.0 km below the flexed lithospheric surface in (c and d), respectively.

which is equivalent to summing the moment of all events $M_0^{(i)}$ which occur in a volume V over a time period τ , scaled by 2 times the shear modulus μ . First, we show the results for volumes spanning the upper 25 km of the lithosphere, and $0.5^\circ \times 0.5^\circ$ bins in latitude and longitude. The seismic strain rate ranges 10^{-20} s^{-1} to 10^{-15} s^{-1} (Figure 1a), is maximal in south-eastern Hawaii, spans ~ 400 km in width, ~ 500 km in length, and reduces to zero beyond Oahu. When the areal bins are enlarged to $1.0^\circ \times 1.0^\circ$ in latitude and longitude, the effect is to smooth the seismic strain rate pattern and reduce the magnitude (Figure 1b). The maximum seismic strain rate is in a good agreement with the back-of-the-envelope calculation for flexural strain rate mentioned prior ($\sim 10^{-15} \text{ s}^{-1}$), suggesting that seismic deformation is representative of lithospheric deformation from flexure.

We compute the seismic strain rate as a function of depth considering events within a 250 km radius centered on Hawaii where the vast majority of events are located. The 1D vertical profile is first computed in discrete 5 km depth bins (Figure 1c), which ranges from 10^{-18} s^{-1} to 10^{-16} s^{-1} in magnitude, and the local minimum at 17.5 km depth constrains the depth of the neutral plane relative to the surface of the flexed lithosphere. Considering a depth-correction of 7–10 km is applied across the Island of Hawaii where the contribution to seismic strain rate is greatest, the neutral plane depth constrained by seismic strain rate relative to sea-level would be 24.5–27.5 km which is slightly deeper than the estimate based on a gap in seismicity (21 km; Klein, 2016), but consistent with the broader range across which seismic focal mechanisms change from radial extension above and radial compression below the neutral plane (20–25 km relative to sea-level; Ross et al., 2007). We emphasize the importance of measuring the neutral plane depth relative to the surface of the flexed plate, since measuring relative to sea-level will overestimate the neutral plane depth by neglecting spatial variations in flexure. In addition, the minimum in seismic strain rate is a more

robust constraint on neutral plane depth than a gap in seismicity which does not consider earthquake size. The seismic strain rate reduces dramatically below ~ 35 km depth and this should not be interpreted as the base of the mechanical lithosphere, but rather as the depth at which brittle failure transitions to ductile deformation due to increasing temperature and pressure (i.e., seismogenic thickness and mechanical thickness are not equivalent).

To reduce sensitivity to error in the earthquake depth-location, we also compute a 10 km vertical moving window average which shallows the depth of the neutral plane from 17.5 to 15 km (Figure 1d). Events which occur beneath Hawaii and the seismic receiver network typically have small uncertainty associated with the depth-location (< 5 km), but events outside the array in map-view may have significantly larger uncertainty. This should not strongly affect our results because the vast majority of events occur beneath Hawaii, but we test the sensitivity of the seismic strain rate to the horizontal region, nonetheless. If we reduce the horizontal radius from 250 to 150 km the seismic strain rate is translated to larger magnitude by \sim half order of magnitude, and the depth of the neutral plane is maintained at 15 km (Figure S1a). The same is true for horizontal averaging radii of 100 km (Figure S1b) and 50 km. The benefit of averaging over a larger areal extent is that larger regions are more likely to be representative of the long-term average strain rate, whereas smaller regions are more likely to have a moment deficit or excess due to the smaller number of events that occur in smaller regions. Results are also quite insensitive to the vertical averaging window for 5–15 km widths (Figure S2).

Longer observation periods have similar benefits to considering larger regions, where longer timescales which exceed the recurrence timescale of the largest events are ideal. However, there is also a drawback to using older data from the twentieth century when observational methods were less advanced. To test the sensitivity of the seismic strain rate to observation period, we also compute the 1D vertical profile for earthquakes recorded over a 20-year period from 2000 to 2019 and compare with the estimates for the 60-year period presented so far. For 10 and 15 km vertical moving window average, the average magnitude of 10^{-17} s^{-1} is reproduced and the depth of the neutral plane is slightly increased from 15 to 20 km and 17.5 km, respectively (Figure S3). Variation in the neutral plane depth may reflect a moment deficit in the reduced time window, and we will consider a range about the neutral plane to accommodate for uncertainty when comparing with model predictions.

3. Viscoelastic Loading Model

In the following, we present the viscoelastic loading model which computes the surface flexure and internal deformation of the lithosphere in response to time-dependent loading from volcanic island building. The model has been developed and used in previous studies (Bellás et al., 2020; Zhong et al., 2003; Zhong & Watts, 2013), but we describe all essential aspects in the following and in the supporting information.

3.1. Governing Equations

The response of an incompressible viscoelastic medium is expressed by conservation of mass and momentum (Wu, 1992; Zhong & Watts, 2013)

$$u_{i,i} = 0, \quad (2)$$

$$\sigma_{ij,j} - (\rho g u_3)_i = 0, \quad (3)$$

where u_i is the displacement vector, σ_{ij} is the stress tensor, ρ the density, g the acceleration due to gravity, and u_3 the vertical component of the displacement vector. We use subscript notation where $A_{,i}$ represents the derivative with respect to x_i , and repeated indices are summed over. The boundary conditions at the four vertical sidewalls and bottom boundary are free-slip, and the top boundary is a deformable free surface subject to time-dependent loads (i.e., the Hawaiian volcanoes)

$$\sigma_{ij} n_j = \sigma_L(x, y, t) n_i, \quad (4)$$

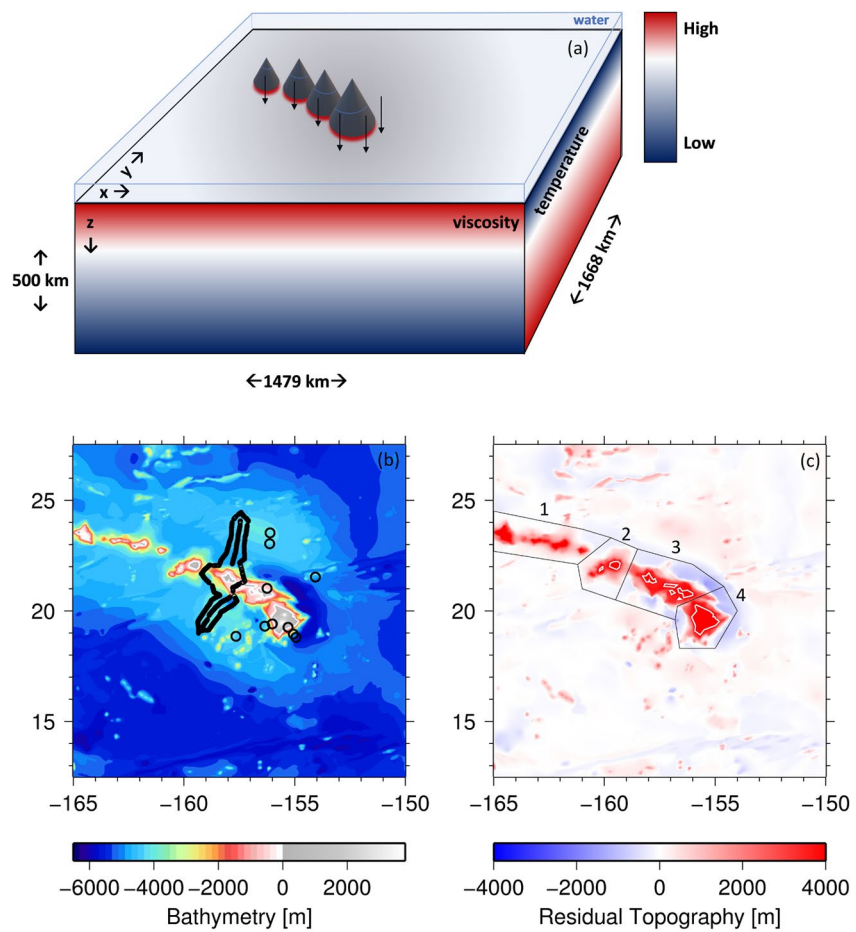


Figure 2. Model schematic, observations of bathymetry, topography, and time-dependent loads (adapted from Bellas et al., 2020). (a) A schematic of the 3D viscoelastic loading model with deformable free surface that is subject to time-dependent loads from Hawaiian Island building. (b) Topography and bathymetry of the Hawaiian Islands and surrounding region. Black circles mark the locations of seismic reflection data which precisely measure flexure. (c) The residual topography derived from correcting the topography and bathymetry in (b) for thermal isostasy, swell topography, and crustal thickness variations. The residual topography represents the load associated with the Hawaiian Islands. The load is divided into four discrete loading regions and applied sequentially. The load in each region is linearly increased over loading periods listed in Table S1.

where n_i is the unit vector normal to the upper surface (Figure 2a).

The loads are based on observations of topography and bathymetry at the Hawaiian Islands (Figure 2b) corrected for thermal isostasy, swell topography, and crustal thickness variations (Figure 2c). The result is the residual topography (Figure 2c) or the static load which is applied in four distinct stages for each of the loading regions (see Figure 2c). The timing of each loading stage is informed by the ages of volcanic rocks and submerged coral reefs (details are presented in Table S1; also refer to Figure 3 in Zhong & Watts, 2013). The deformable free surface is also subject to dynamic loads from volcanic, sediment, or water infill as the surface deflects (refer to Table 2 for associated densities).

The model geometry is a 3-D Cartesian box with dimensions of 1,479 km in x (east-west), 1,668 km in y (north-south), and 500 km in z (depth) (Figure 2a). The horizontal domain is consistent with a region ranging $\theta = 12.5\text{--}27.5^\circ\text{N}$ and $\phi = 165\text{--}150^\circ\text{W}$, based on $x = R(\phi - \phi_1)\cos\theta_2\pi/180$, $y = R(\theta - \theta_1)\pi/180$, where $\phi_1 = 165^\circ\text{W}$, $\theta_1 = 12.5^\circ\text{N}$ and $\theta_2 = 27.5^\circ\text{N}$. The grid resolution is $128 \times 128 \times 32$ elements in the horizontal (x), horizontal (y), and vertical (z) dimensions, respectively. Significant grid refinement is applied in the upper 50 km where elements are 2.5 km in the vertical dimension, and moderate horizontal grid refinement around the domain center where the Hawaiian Islands are located is applied such that elements are

Table 2
Model Parameters

Parameter	Value
Shear modulus, μ	7×10^{10} Pa
Gravitational acceleration, g	9.8 m/s^2
Gas constant, R	8.32 J/(mol K)
Mantle density, ρ_m	$3,330 \text{ kg/m}^3$
Volcanic and/or crustal density, ρ_c	$2,800 \text{ kg/m}^3$
Sediment density, ρ_s	$2,300 \text{ kg/m}^3$
Water density, ρ_w	$1,030 \text{ kg/m}^3$
Mantle Temperature, T_m	$1,350^\circ\text{C}$
High-temperature creep (Podolefsky et al., 2004)	
$\eta = \frac{\sigma}{\dot{\epsilon}} = \frac{\eta_0}{1 + (\sigma / \sigma_T)^{n-1}} \exp\left(\frac{E_c}{RT} - \frac{E_c}{RT_m}\right)$	
Stress exponent, n	3.5
Activation energy, E_c	360 kJ/mol
Transition stress, σ_T	3×10^5 Pa
Reference viscosity, η_0	10^{20} Pa s
Low-temperature plasticity (Idrissi et al., 2016)	
$\eta = \frac{\sigma}{\dot{\epsilon}} = \frac{\sigma}{B} \exp\left\{\frac{E_p}{RT} \left[1 - \left(\frac{\sigma}{\sigma_p}\right)^p\right]^q\right\}$	
Pre-exponential factor, B	10^6 s^{-1}
*Activation energy, E_p	566 kJ/mol
Peierls stress, σ_p	3.8 GPa
Stress exponent, m	0
Stress exponent, p	1/2
Stress exponent, q	2
Frictional sliding (Byerlee, 1978)	
$\eta = \frac{\tau_{\text{yield}}}{\dot{\epsilon}} = \frac{\mu_f \sigma_n}{\dot{\epsilon}}$	
*Frictional coefficient, μ_f	0.7

Note. The parameters marked with * are varied in the model to test their influence on flexure and the distribution of stress and strain (Table 3).

$\sim 10 \times 10 \text{ km}^2$. The grid is Lagrangian which is important for the convergence of the governing equations of viscoelastic deformation (i.e., the elastic force component is proportional to displacement).

3.2. Rheological Equations

For an incompressible Maxwellian medium, the stress tensor is given by (e.g., Zhong & Watts, 2013)

$$\sigma_{ij} + \frac{\eta}{\mu} \dot{\sigma}_{ij} = -\left(p + \frac{\eta}{\mu} \dot{p}\right) \delta_{ij} + 2\eta \dot{\epsilon}_{ij}, \quad (5)$$

where η is the viscosity, μ the shear modulus, P the pressure, and $\dot{\epsilon}_{ij}$ the strain rate tensor. The time-derivatives of stress and pressure in Equation 5 distinguish it from purely viscous rheology. The elastic properties are uniform throughout the domain (constant $\mu = 7 \times 10^{10}$ Pa; Table 2) but the viscosity is defined by one of the three deformation mechanisms depending on local temperature and stress. The rheology of high-temperature creep, low-temperature plasticity, and frictional sliding are formulated in terms of strain rate or yield stress following the experimental studies, and converted to viscosity in the viscoelastic loading model following $\eta = \sigma / \dot{\epsilon}$ (Table 2; Supporting Information). A maximum and minimum viscosity of 10^{27} Pa s and 10^{21} Pa s are imposed for computational efficiency, respectively.

Wherever temperature exceeds a threshold value, viscosity is defined by high-temperature creep in a composite form including diffusion and dislocation creep, although we neglect the effects of dynamic grain-size evolution in the present study (e.g., Podolefsky et al., 2004)

$$\dot{\epsilon} = A\sigma\left(\sigma_T^{n-1} + \sigma^{n-1}\right)\exp\left(-\frac{E_c}{RT} + \frac{E_c}{RT_m}\right) \quad (6)$$

where $\dot{\epsilon}$ is the second invariant of the strain rate tensor, σ is the second invariant of the deviatoric stress tensor, A is a pre-factor, n is the stress exponent, σ_T is the transition stress at which diffusion and dislocation creep contribute equal strain rate, E_c is the creep activation energy, and T_m is the mantle temperature (Table 2). The viscosity based on Equation 6 is derived in supporting information and presented in Table 2. The threshold or activation temperature is important because high-temperature creep is limited by diffusional processes and therefore fundamentally limited by thermal activation. In any case, Zhong and Watts (2013) demonstrated that the amplitude of flexure is largely insensitive to high-temperature creep for reasonable asthenospheric viscosity (10^{20} – 10^{22} Pa s) because it predominantly controls the timescale of stress relaxation in the weak underlying mantle, not lithospheric stresses which support the loads.

For this reason, we do not vary rheological parameters associated with high-temperature creep and use $E = 360$ kJ/mol for all models to be consistent with field-based studies on sub-lithospheric small-scale convection (van Hunen et al., 2005), and set the threshold activation temperature $T = 800^\circ\text{C}$.

Wherever temperature is less than the threshold value (800°C), viscosity is defined by the smaller of those predicted by frictional sliding and low-temperature plasticity. In this sense, no threshold temperature for the transition between low-temperature plasticity and frictional sliding is imposed, rather, the transition is determined dynamically in the model. Low-temperature plasticity takes an exponential form (Goetze & Evans, 1979; Idrissi et al., 2016)

$$\dot{\epsilon} = B\sigma^m \exp\left\{-\frac{E_p}{RT}\left[1 - \left(\frac{\sigma}{\sigma_p}\right)^p\right]^q\right\}, \quad (7)$$

in which B is the pre-factor, m the stress exponent, E_p is the plastic activation energy, R the universal gas constant, T the temperature, σ_p the Peierls stress or resistance to dislocation glide, and the exponents p and q control sensitivity to stress (Tables 2 and 3). The viscosity predicted by low-temperature plasticity is formulated in terms of stress (Table 2) which is solved dynamically on each time step.

Finally, the yield stress of frictional sliding increases with depth following Byerlee's law according to experiments (Byerlee, 1978)

$$\tau_{yield} = \mu_f \sigma_n \quad (8)$$

Since we do not explicitly consider the effects of pore-pressure, μ_f throughout this study is the effective frictional coefficient.

We will vary the value of the frictional coefficient to test which value best reproduces observations of flexure and the seismic strain rate. As was mentioned in the Introduction, previous studies have shown that the flexure is predominantly controlled by the strength of low-temperature plasticity, but there is some trade-off with frictional sliding. In addition to the frictional coefficient, we will also vary the strength of low-temperature plasticity based on the requirement that the observed flexure is reproduced to within a misfit of ~ 0.3 , which is the minimum misfit this type of modeling can produce (Bellas et al., 2020; Zhong & Watts, 2013). Since flexure is predominantly controlled by low-temperature plasticity, we expect that only small variations in the yield stress of low-temperature plasticity will be required to balance more significant variations in the frictional coefficient. Within this set of models, significant variations in the frictional coefficient are expected to produce significant variations in the distribution of stress and strain at shallow depths. In other words, many combinations of frictional sliding and low-temperature plasticity will reproduce the observed flexure, but only a few of these will also reproduce the seismic strain rate where the model strain rate at shallow depths is controlled by frictional sliding. In general, the effective elastic thickness of the model lithosphere is constrained by observations to be ~ 30 km. The effect of varying the frictional coefficient between models will be to perturb the distribution of strength in the lithosphere (but not the net strength), which will then be compared with the seismic strain rate. We acknowledge that uniformly varying the frictional coefficient does not account for strain localization on fault planes in the real Earth (e.g., Wolfe et al., 2003) or strain softening (Huisman & Beaumont, 2003; Meyer et al., 2017; Naliboff et al., 2020). Our objective is to estimate the averaged and smoothed value of the frictional coefficient based on a comparison of the strain rate in numerical models and the seismic strain rate, both of which act to smooth and average lithospheric deformation. Future studies will be necessary to explore the effects of spatial variations in μ_f , including dynamic strain softening, but this is beyond the scope of the present work.

We choose to modify the strength of low-temperature plasticity by modifying the activation energy, E_p . Previous studies have reproduced observations of flexure by modifying E_p or the pre-factor, A , with equal success (Bellas et al., 2020; Zhong & Watts, 2013). Although modifying a single parameter value destroys the fit to laboratory data, it is not necessarily clear that the rheological parameter values which apply at laboratory conditions (e.g., strain rate $\sim 10^{-6}$ s $^{-1}$) also apply at lithospheric conditions (e.g., strain rate $\sim 10^{-16}$ s $^{-1}$). Nonetheless, it has been proposed that a more sophisticated multivariate approach which preserves the fit to laboratory or field data while also reproducing flexure at lithospheric conditions is preferred (Jain et al., 2017; Reuber et al., 2020). While it is beyond the scope of the present study to perform a multivariate approach to modifying laboratory-derived flow laws, the reduction in strength required to reproduce observations of flexure is identical regardless of whether one or many variables are varied in the laboratory-derived flow law. Therefore, it is our objective to offer insight into the distribution of strength that reproduces observations rather than an absolute constraint on the value of any particular rheological parameter in the formulation of low-temperature plasticity. In contrast, the yield stress of frictional sliding is controlled by a single parameter, μ_f , so that no such ambiguity applies and the value of μ_f may be constrained uniquely.

Table 3
Model Input Parameters and Output

Case	μ_f	E_p [kJ/mol]	Misfit to flexure	Neutral plane depth [km]	Misfit to seismic strain rate
Model 1	0.7	400	0.293	15	1.4
Model 2	0.4	410	0.289	15	0.8
Model 3	0.15	445	0.296	25	2.6
Model 4	0.1	460	0.293	30	19.7
Model 5	0.2	430	0.289	20	1.7
Model 6	0.05	480	0.270	35	157.3
Model 7	0.6	400	0.289	15	1.3
Model 8	0.5	400	0.285	15	1.2
Model 9	0.3	420	0.291	20	0.8

Note. In low-temperature plasticity from Idrissi et al. (2016), the published value $E_p = 566$ kJ/mol.

We must also address that other studies have suggested lab-derived low-temperature plasticity is perfectly consistent with Earth's lithosphere, and rather does not reproduce observations of flexure at Hawaii because thermal erosion by the Hawaiian plume significantly weakens the Hawaiian lithosphere by modifying the ~ 90 Myr thermal structure (Guest et al., 2020; Hunter & Watts, 2016; Pleus et al., 2020). This would cause viscoelastic loading models to overestimate lithospheric strength and underestimate flexure if they do not account for the anomalous thermal structure. However, this topic is controversial and other studies have also suggested the opposite view: that thermal modification does not significantly alter the shallow part of the lithosphere based on seismic tomography (Laske et al., 2011), a lack of heat flux anomalies (von Herzen et al., 1989), thermal convection models (Ribe & Christensen, 1994), and plume-induced thermal anomalies in viscoelastic loading models (Bellas et al., 2020). The strongest argument against significant thermal modification to Hawaiian lithosphere is that the effective elastic thickness is not anomalous compared to other Pacific lithosphere of similar age (e.g., 30–35 km) (Watts & Zhong, 2000). Therefore, our preferred view is that the thermal effects of the plume and magmatism must be highly localized compared to the large spatial scale of flexure (400 km wavelength). On

this basis, we ignore thermal anomalies and apply the cooling half-space model to compute the temperature profile in the model lithosphere

$$T = T_0 + \Delta T \operatorname{erf} \left(\frac{z}{2\sqrt{\kappa t_s}} \right) \quad (9)$$

where erf is the error function, z is depth, t_s is the local age of the crust and κ is the thermal diffusivity. Since the governing equations of the model include conservation of mass and momentum but not energy, the thermal structure does not evolve dynamically except by deformation of the Lagrangian grid due to flexure. We do not expect the buoyancy field to evolve appreciably on the timescales associated with flexure at the Hawaiian Islands (<5 million years).

Since thermal erosion of the lithosphere may not impart significant weakening to the shallow part of the lithosphere nor affect flexure modeling results (Bellas et al., 2020), modification of lab-derived low-temperature plasticity is required to reproduce observations of flexure at the Hawaiian Islands. The constraint which dictates the degree of weakening is the integrated strength of the model lithosphere which must reproduce the observed flexure when subjected to loading consistent with Hawaiian Island building. This is equivalent to predicting an effective elastic thickness of 30–35 km. The integrated strength is jointly controlled by frictional sliding (μ_f), low-temperature plasticity (E_p) and the elastic strength (μ), but high-temperature creep has a weak or negligible influence. Forward modeling provides a quantitative constraint on lithospheric rheology because μ is well-constrained, μ_f and E_p are jointly constrained with some trade-off by flexure, and μ_f and E_p are jointly constrained to a unique pair-value by the seismic strain rate.

4. Model Results

The viscoelastic loading models compute the deformational response of the lithosphere to the building history of Hawaiian Islands from west of Kauai to Hawaii. We analyze the model predictions for present-day and compare them with observations of flexure, seismic strain rate (Section 4.1) and the stress field from seismic observations (Section 4.2) to constrain μ_f and low-temperature plasticity.

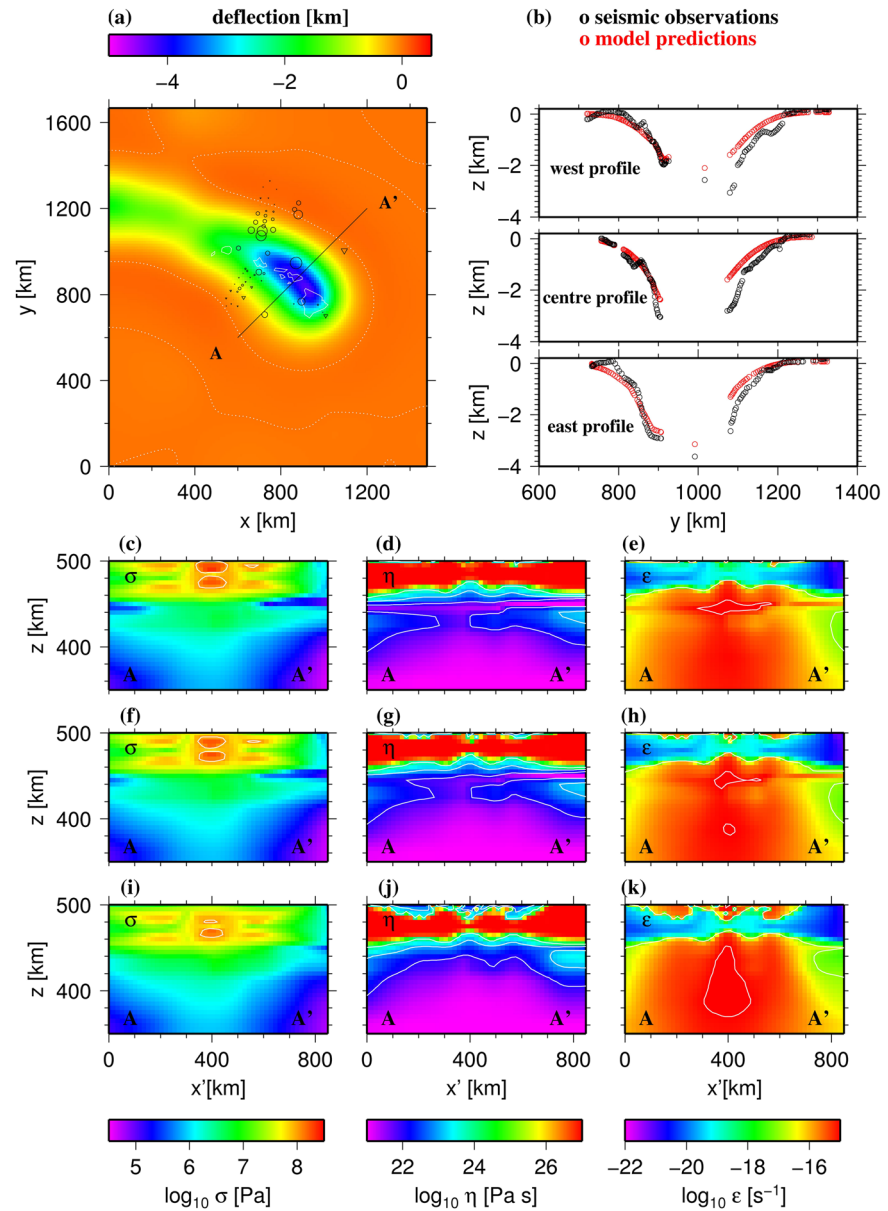


Figure 3. Predicted flexure, stress, viscosity, and strain rate. The surface flexure from Model 1 in map-view (a), and in cross-section compared to seismic observations (b). The size of symbols superposed on (a) represent the difference between predicted and observed flexure, with circles for underpredictions and triangles for overpredictions (magnitude shown in b). In the rows below, we show cross-sections along the transect marked AA' of stress (σ), viscosity (η), and strain rate ($\dot{\epsilon}$) for Model 1 with $\mu_f = 0.7$ (c–e), Model 2 with $\mu_f = 0.4$ (f–h), and Model 3 with $\mu_f = 0.15$ (i–k). Contours on panels (c–k) show the iso-lines on which stress is 100 MPa, viscosity is 10²² Pa s, and strain rate is 10⁻¹⁵ s⁻¹.

4.1. Constraints on the Frictional Coefficient

The locations of flexure data from seismic reflections are shown by circles (Figure 2b) and symbols (Figure 3a) and those flanking Oahu are also shown in cross-section (Figure 3b). These observations are also presented in more detail in previous studies (Bellas et al., 2020; Zhong & Watts, 2013).

In Model 1, we set the frictional coefficient $\mu_f = 0.7$ consistent with mineral physics experiments, and the plastic activation energy is reduced from 566 kJ/mol (Idrissi et al., 2016) to $E_p = 400$ kJ/mol to reproduce the flexure at Hawaii (Table 3). The predicted flexure is nearly 5 km at Hawaii and produces a misfit of ~ 0.3 with observed flexure, which is about the minimum misfit that this type of model can achieve (Table 3;

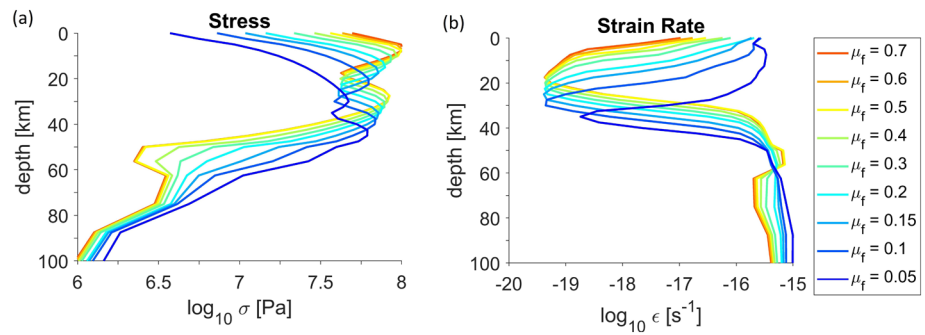


Figure 4. Vertical profiles of predicted second invariants of stress and strain rate. The 1D vertical stress (a) and strain rate (b) profiles from viscoelastic models averaged within a 250 km radius centered on Hawaii. The depth of the neutral plane is constrained by the minimum in either stress or strain rate, which increases with decreasing μ_f , but approaches 18 km for $\mu_f \geq 0.5$. Depth represents depth relative to the surface of the flexed model lithosphere.

Figures 3a and 3b; Bellas et al., 2020; Zhong & Watts, 2013). Stresses are concentrated in the upper ~ 35 km with a maximum value of ~ 100 MPa (Figure 3c). Viscosity is uniformly large (10^{27} Pa s) in the upper 35 km, except where nonlinearity of the rheology produces weakening, such that directly beneath the load the high viscosity layer thins to 30 km thickness (Figure 3d). The maximum magnitude of viscosity (10^{27} Pa s) is caused by imposing an upper bound in the model; otherwise, the viscosity could be even higher (but with no physical effect, because such highly viscous material is already essentially elastic on the timescale of Hawaiian Island building). The strain rate is small and $< 10^{-18}$ s $^{-1}$ in the upper ~ 35 km, except for isolated shallow patches where it approaches 10^{-16} s $^{-1}$ due to deformation by frictional sliding. Strain rate is largest ($> 10^{-16}$ s $^{-1}$) directly beneath the load and at the base of the lithosphere due to viscous creep deformation (Figure 3e).

In Model 2, the frictional coefficient is $\mu_f = 0.4$, and the plastic activation energy is set to $E_p = 410$ kJ/mol. Model 2 reproduces the observations of flexure equally well (Table 3), but differs from Model 1 in that lithospheric stresses are concentrated at larger depths (5–40 km), shallow nonlinear-weakening of the viscosity is enhanced, and shallow zones of high strain rate within the lithosphere are increased in size and amplitude (10^{-15} s $^{-1}$; Figures 3f–3h). These effects are magnified further in Model 3 with $\mu_f = 0.15$ and $E_p = 445$ kJ/mol, which again reproduces the observed flexure equally well as Models 1 and 2 (Table 3), but lithospheric stresses are concentrated between 10 and 45 km depth (Figure 3i), nonlinear weakening significantly reduces viscosity in the upper 20 km within ~ 200 km of the load (Figure 3j), and high strain rates (10^{-15} s $^{-1}$) occur throughout this shallow weak region (Figure 3k). Additional models with different μ_f from 0.05 to 0.7 and activation energy, E_p , are also computed (Table 3). These models demonstrate that variation of μ_f strongly affects the depth-distribution of stress and strain rate, and reduction of μ_f significantly weakens the shallow lithosphere.

The effect of μ_f on the vertical distributions of second invariants of stress and strain rate is demonstrated more clearly by the 1D vertical profiles averaged within a 250 km radius centered on Hawaii. Stresses exhibit a local minimum (i.e., the neutral plane) at shallower depths for increasing μ_f (Figure 4a) but begin to overlap for $\mu_f \geq 0.5$. Strain rates reduce to a minimum value at the same depth as stresses (Figure 4b). The depth of the neutral plane increases from 17.5 km for $\mu_f = 0.7$, to 35 km for $\mu_f = 0.05$ (Table 3). Deepening of the neutral plane occurs because the shallow lithosphere is very weak for small μ_f , so the stresses required to support the load of the Hawaiian Islands must migrate to larger depths.

The magnitude of strain rate at the neutral plane depth is always much lower in the models compared to the seismic estimate (Figure 5), and this is not particularly surprising considering the models are formulated to consider forcing from surface loads and a homogeneous lithosphere, which neglects natural small-scale variations in composition, temperature, loading, background stress, magmatism, error in earthquake depth-location, etc., which may affect the observed seismic strain rate (McGovern, 2007; Pritchard et al., 2007). However, we do expect for model and seismic strain rate to agree where the strain rate magnitude is large (at the surface and 25–30 km depth).

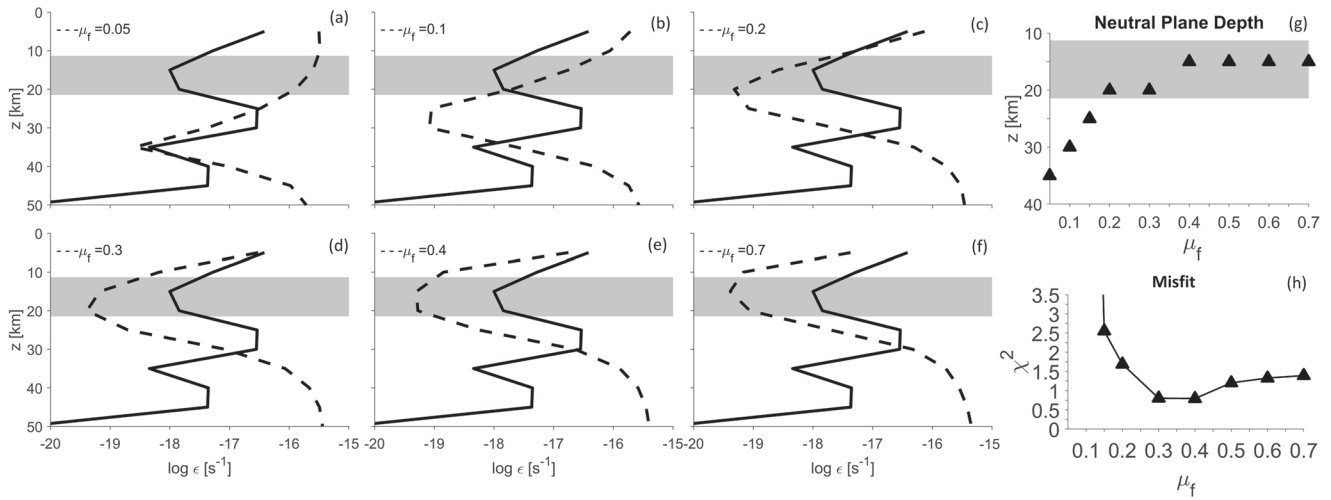


Figure 5. The strain rate, neutral plane depth, and misfit of seismic observations and predictions. (a–f) The 1D vertical strain rate profile from seismic observations (solid) and numerical models with varying frictional coefficient μ_f (dashed). Depth, z , represents depth within the lithosphere relative to the flexed crustal surface. Strain rates are averaged within a 250 km radius centered on Hawaii, averaged vertically within 10 km moving windows, and the gray bar depicts a factor of ~ 3 variation about the minimum seismic strain rate. (g) The minimum seismic strain rate locates the neutral plane at ~ 15 km depth which is reproduced only by models with $\mu_f \geq 0.2$. (h) The χ^2 misfit for seismic strain rate is minimized for $\mu_f = 0.3$ – 0.4 for depths 0–30 km the lithosphere, which constrains the value representative of the Hawaiian lithosphere.

Comparison of model predictions with the seismic strain rate provides a constraint on the magnitude of μ_f because it strongly influences the vertical distributions of stress and strain. The 1D vertical profiles of predicted and seismic strain rates do not agree for $0.05 \leq \mu_f < 0.2$. The shallow model lithospheres are too weak, the shallow model strain rates are too high, and the model neutral planes are too deep, compared to the seismic estimate for $\mu_f < 0.2$ (Figures 5a and 5b). However, for $0.2 \leq \mu_f \leq 0.7$, the model neutral plane depths are within ± 5 km of that based on the seismic strain rate (Figures 5c–5g).

Although all of these models with $0.2 \leq \mu_f \leq 0.7$ reproduce the neutral plane depth from seismic strain rate, some reproduce the magnitude of seismic strain rate better than others. To test the agreement between model and the seismic strain rates, we compute the χ^2 misfit,

$$\chi^2 = \frac{1}{N} \sum_{i=1}^N \left[\frac{S_i - M_i}{std(S_i)} \right]^2 \quad (10)$$

where N is the number of depth bins for seismic strain rate (Figure 5), s_i is seismic strain rate at each depth, M_i is model strain rate at each depth and std is the standard deviation. The χ^2 misfit is calculated for depths ≤ 30 km because the seismic strain rate significantly reduces below this depth. The misfit shows that the magnitude of the seismic strain rate is best reproduced by $\mu_f = 0.3$ – 0.4 , which provides a constraint on the preferred value of the effective frictional coefficient in the Hawaiian lithosphere (Figure 5h).

Next, we test whether this constraint is robust against different averaging techniques and misfit methods. If the areal extent is reduced from 250 km to 150 or 100 km, the neutral plane depth and misfit prefer models with $\mu_f = 0.2$ – 0.4 (Figure S1). If the vertical averaging windows are changed from 10 to 5 km or 15 km, the preferred models have $\mu_f = 0.3$ or $\mu_f = 0.3$ – 0.4 , respectively (Figure S2). If the observation period is reduced from 1960–2019 to 2000–2019, the seismic strain rate subject to either a 10 km or 15 km vertical moving window average is best reproduced by models with $\mu_f = 0.3$ – 0.4 (Figures S3a and 3b), although the misfit seems to be affected by a moment deficit and high sensitivity to overestimates in these cases (see supporting information Discussion). If the misfit is formulated differently, the preferred model has $\mu_f = 0.3$ for 5, 10, and 15 km vertical window averages (Figures S4a–4c). Therefore, the most robust constraint based on the neutral plane depth and misfit of seismic and model strain rates is $\mu_f = 0.3 \pm 0.1$, and this result is resilient against variations in areal extent, vertical averages, observation period for seismic data, and misfit formula.

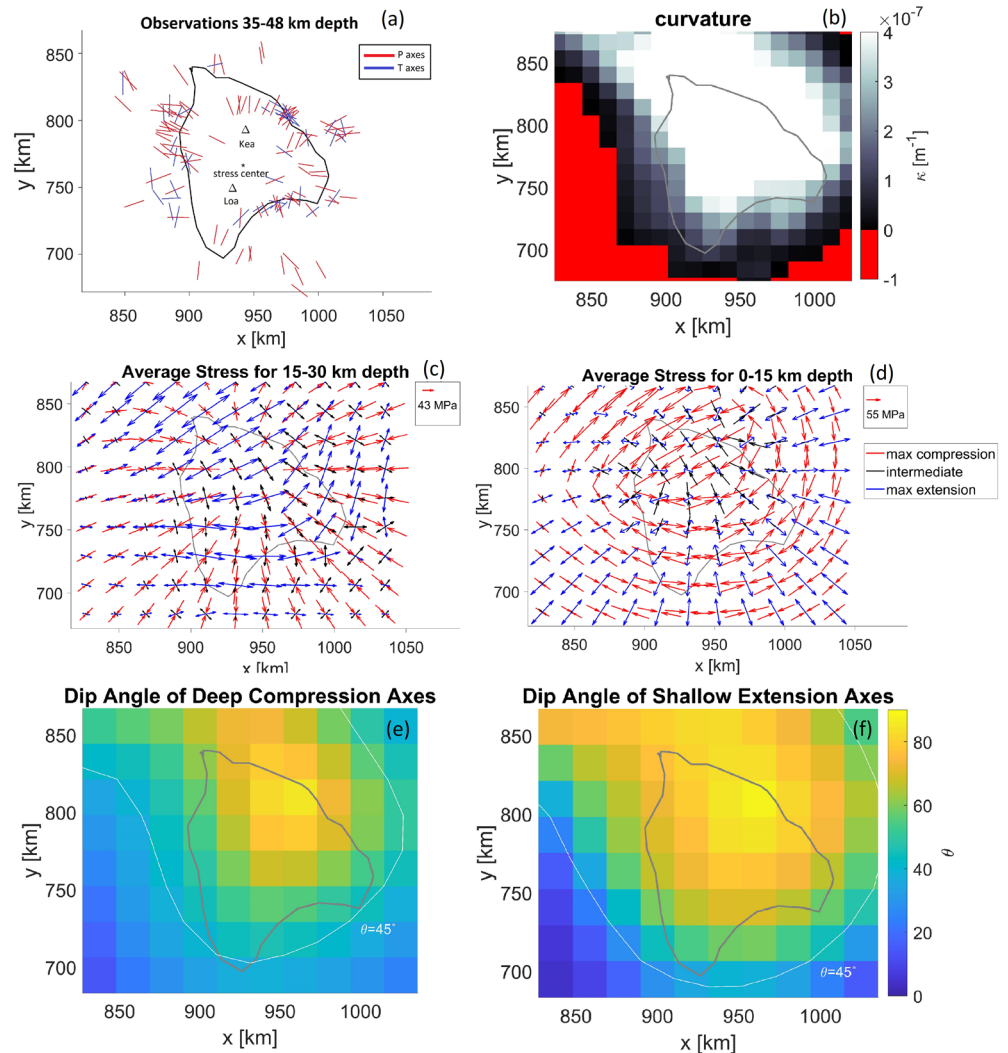


Figure 6. Observed P and T axes and predicted principal stresses. (a) Modified from Klein (2016), the observed pressure (P) and tension (T) axes with dip angle $<45^\circ$ and below the neutral plane. (b) Curvature or the second-order derivative of the model surface deflection. Curvature that is concave down is negative in this coordinate frame and concave up is positive. (c) and (d) The predicted axes of maximum compressional (red), intermediate (black) and extensional (blue) stresses below (c) and above (d) the neutral plane for the best-fit Model 9 with $\mu_f = 0.3$. The dip angle of (e) deep radial compression axes averaged below the neutral plane and (f) shallow radial extension axes averaged above the neutral plane with a contour to show the location at which the dip angle crosses 45° .

4.2. Load-Induced Lithospheric Stress

We present the principal stresses for our preferred Model 9 with $\mu_f = 0.3$ and compare with seismic observations of P and T axes (Klein, 2016). As discussed in Section 2, Klein (2016) demonstrated that earthquakes deeper than the neutral plane (21 km below sea level) consistently produce P axes that point radially toward a stress center located in central Hawaii between Mauna Kea and Mauna Loa (Figure 6a). Tangential T axes are also observed below the neutral plane, but such observations are less robust than radial P axes. For Model 9, the predicted stress field below the neutral plane (20–40 km) is dominated by radial compression and tangential extension axes relative to the load-center in central Hawaii (Figure 6c). The predicted stress field above the neutral plane (0–20 km) is dominated by radial extension and tangential compression (Figure 6d) which is largely opposite to stresses below the neutral plane. Therefore, the predictions are generally consistent with first order observations of deep radial P axes and tangential T axes relative to a stress center between Mauna Kea and Mauna Loa.

In greater detail, radial extension and compression axes are dominantly horizontal at distances >50–100 km from the stress center to the northeast, southeast, and southwest, and the implied focal mechanism would be strike-slip (Figures 6c–6f). The dip angle exceeds 45° and the radial axes become dominantly vertical for distances <50–100 km around the stress center which would imply a transition from strike slip to normal faulting below, and reverse faulting above the neutral plane, respectively (Figures 6e and 6f). The location where dip angle exceeds 45° also coincides with the transition in surface curvature from concave down to concave up, a feature expected for the flexure of a coherent plate (Figure 6b). Asymmetry to the northwest due to loading from older Hawaiian Islands is reflected by stress axes which are dominantly vertical even for distances >50–100 km from the stress center, implying focal mechanisms along the island chain are normal and reverse below and above the neutral plane, respectively. Tangential axes are preserved and perpendicular to the island chain in the region to the northwest.

The predicted stress field is qualitatively consistent with observations of increasing dip angle of radial *P* axes approaching the stress center, but quantitatively inconsistent: the dip angles predicted by our model are significantly larger than those observed. How this disagreement should be interpreted is complicated by the fact that Klein discarded dominantly vertical *P* axes (dip angle >45°) on the basis that the radial component solution is not as reliable for such events (discussed in detail in Section 5.2).

5. Discussion

5.1. Coefficient of Friction

Constraints from the depth of the neutral bending plane and the misfit between seismic and model strain rates show the preferred value of the frictional coefficient $\mu_f = 0.3 \pm 0.1$. Previously, Zhong and Watts (2013) constrained $\mu_f \geq 0.25$ based on a similar comparison with the neutral plane depth from seismicity. There are two important distinctions to note between their work and the present study: (i) Zhong and Watts estimated the neutral plane depth based on seismicity rather than seismic strain rate, and (ii) Zhong and Watts compared the depth distribution in models, which is measured relative to the surface of the bending lithosphere, to the depth of minimum seismicity, which is measured relative to sea-level. This discrepancy is corrected in the present study. We present a more robust and precise estimate of the frictional coefficient in the present study ($\mu \sim 0.3$), which is consistent with Zhong and Watts (2013).

Observations of flexure and seismic strain rate constrain $\mu_f \sim 0.3$ which is small compared to: estimates from mineral physics experiments which constrain $\mu_f = 0.5$ –0.85 (Boettcher et al., 2007; Byerlee, 1978), in situ borehole measurements of stress on intraplate continental faults which constrain $\mu_f = 0.6$ (Zoback & Townend, 2001), and models of normal faults at subduction zones which constrain $\mu_f = 0.6$ –0.85 (Billen et al., 2007). Our estimate is approximately consistent with estimates based on the dip angles of newly formed normal faults at subduction zones which constrain $\mu_f < 0.3$, but larger than $\mu_f < 0.1$ as constrained by modeling earthquake focal mechanisms for active transform faults at fracture zones (Behn et al., 2002). Our estimate is at least a factor of 3 larger than μ_f required by surface heat flux at plate boundary interfaces $\mu_f < 0.1$ (England, 2018; Gao & Wang, 2014) and by geodynamic models in which plate tectonics emerges (Moresi & Solomatov, 1998). This suggests plate interfaces are much weaker than plate interiors and may indicate that dynamic weakening by chemical and/or mechanical alteration (i.e., strain-softening) is essential to understanding the style and timescale of bending, subduction, and even the origin of plate tectonics.

To test our hypothesis of strong damage-induced weakening, we also compute the seismic strain rate as a function of radial distance from the center of seismic activity in the Hawaiian region. The seismic strain rate is averaged in concentric annuli centered on Hawaii and in the upper 20 km (Figure 7a). The seismic strain rate is larger than the strain rate from all models for 0–50 km radius, but smaller than all models at distances >300 km (Figure 7b). This suggests the effective frictional coefficient may be less than 0.05 at the load-center but significantly larger beyond 300 km distance, which is consistent with our localized weakening hypothesis.

An intuitive explanation for localized weakening in the brittle regime seems to be that increased temperatures due to magmatic intrusion weaken faults in this region. However, recent studies report that frictional sliding is unlike ductile deformation mechanisms which weaken with temperature, and that increased temperatures actually increase the effective strength of frictional sliding by increasing the areal contact of

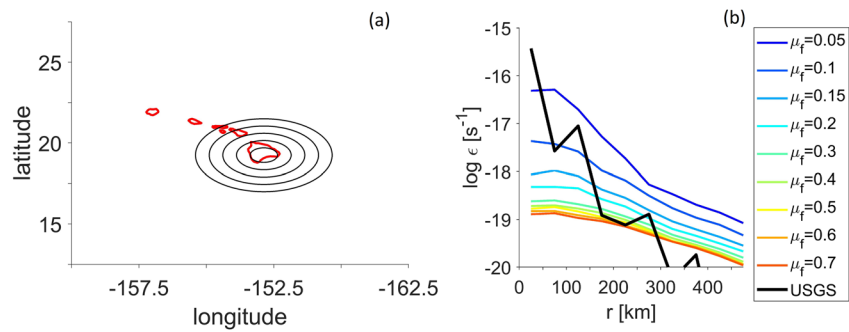


Figure 7. Radial distribution of strain rate. The strain rate is averaged in the upper 20 km in depth and horizontally within annuli centered on Hawaii (a). The steeper slope of seismic strain rate relative to model predictions may suggest the frictional coefficient of the Hawaiian lithosphere is spatially variable and reduces in response to active deformation at central Hawaii (b).

faults (Molnar, 2020). Therefore, increased temperatures would not weaken the brittle regime, but could shallow the depth of the brittle-ductile transition to induce local weakening there and explain the region of low seismicity surrounding the stress center. This could also help to explain the dominantly horizontal P axes by imposing a local weak hole but would fail to explain the high seismic strain rate and apparent reduction in μ_f at central Hawaii (Figure 7).

A source of weakening that could explain all three observations (the low-seismicity zone, horizontal radial P axes and high seismic strain rate) is that damage occurs by deformation-induced weakening (i.e., strain softening). This could reduce the effective frictional coefficient beneath Hawaii and in other tectonic settings such as on the plate boundary interface. The microphysics of such damage, and the potential effects of serpentinization and other hydrous and/or anhydrous reactions to cause such weakening are actively pursued by the mineral physics (e.g., Chernak & Hirth, 2010; Hansen et al., 2020) and mantle dynamics (Bercovici & Ricard, 2014) communities. We suggest a higher likelihood for mechanical or dynamic weakening effects at Hawaii, where mechanisms for chemical alteration by hydration and serpentinization are not as well-established compared to subduction zones.

Apparent lateral variation in brittle strength may also be related to the differing yield stresses of normal, strike-slip and reverse faulting. It is not straightforward to consider the effects of different fault-type strengths (normal, strike-slip and reverse faulting) in 3D geometry, but we do not suspect this has a strong impact on our results because the differences in yield stress are small for small values of μ_f (e.g., $\mu_f = 0.3$) which are preferred by our model results (Figure S5). The fault mechanism-insensitive formulation of brittle yield stress (Equation 8) is approximately consistent with the yield stress of strike slip faults, which are stronger than normal faults but weaker than reverse faults (Figure S5). The different strengths of normal, strike-slip and reverse faults would imply weakening below the neutral plane approaching the stress center, due to a transition from strike-slip to normal faulting and could help explain apparent weakening approaching the stress center. Conversely, a transition from strike-slip to reverse faulting above the neutral plane would imply strengthening, opposite to the apparent weakening suggested by large seismic strain rate at shallow depths (Figure 7). It will be necessary to test spatially varying frictional coefficient and fault mechanism-sensitive yield stress against observations at the Hawaiian Islands in future studies.

While it is possible that the maximum seismic strain rate is augmented by contamination from earthquakes associated with deep magmatism below Kilauea, the magnitude ($\dot{\epsilon} < 10^{-15} s^{-1}$) is consistent with our simplified estimate of strain rate presented earlier and therefore likely represents flexural deformation. We also acknowledge that the reduction in seismic strain rate with distance from Hawaii could also be augmented by an incomplete seismic catalog where small and distant events may be undetected, but small undetected events would contribute very little to strain rate which is exponentially related to earthquake magnitude. Therefore, we suggest the strain rate as a function of radial distance shows strong evidence for weakening near Hawaii, and it will be necessary to test whether lateral variations in μ_f improve the fit to flexure, stress and seismic strain rate in future studies. Lateral variations may be formulated to arise dynamically in the

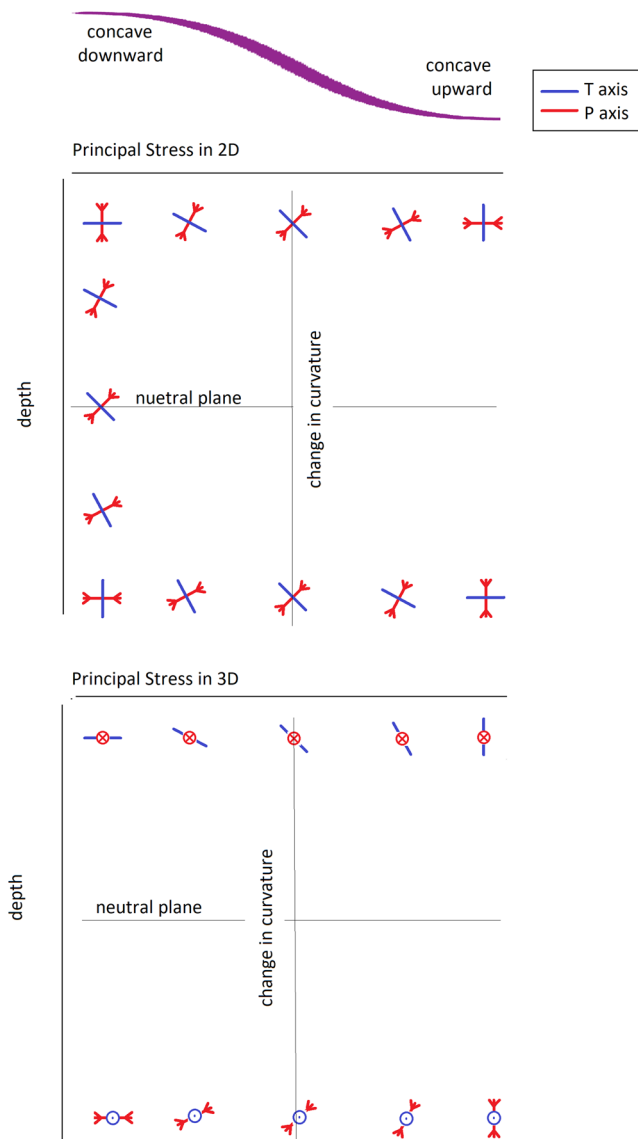


Figure 8. Principal stresses across a change in curvature for 2D and 3D geometry. Principal stresses are shown in a cross-section of the bending plate, where the horizontal dimension is radial relative to the load, and the dimension into or out of the page is tangential. (a) Predictions based on a 2D model are confined to the plane of the page and thus cannot reproduce any stress components tangential to the load. In addition, the 2D model predicts that deep radial compression transitions to deep radial extension across a change in curvature. (b) In contrast, 3D models predict that deep radial compression transitions to deep vertical compression across a change in curvature, with no change to the extensional axis.

model via strain softening criteria, where accumulated strain is tracked and used to prescribe time- and space-dependent reduction in μ_t .

5.2. Lithospheric Stress

Comparison of the principal stresses predicted in models with the observed P and T axes in the Hawaiian lithosphere provides an additional constraint on lateral variations in strength. Whether a change in the surface curvature occurs or not is controlled by the lateral strength distribution of the lithosphere around the load. In particular, we expect for unbroken or coherent plates to exhibit a change in curvature approaching the load (i.e., from concave-down to concave-up), and localized weakening beneath the load would act to reduce the radial distance at which a change in curvature occurs, in contrast to broken plates which would have uniformly concave-down curvature. The change in curvature (or lack thereof) controls the orientation of principal stresses and comparison with observations of P and T axes constrains the lateral strength distribution of the lithosphere. In the following, we first review the 2D model of principal stresses that in part led Klein to conclude the lithosphere is broken and compare with new 3D predictions. Second, we discuss whether the 3D results support an effectively broken lithosphere at Hawaii (i.e., no change in curvature).

Klein compared observations of P and T axes with principal stresses predicted by a 2D model of elastic bending. The principal stresses from a 2D model of elastic bending are shown in Figure 8a, which for concave-downward curvature predicts: (i) above the neutral plane, radial extension (T) axes and (ii) below the neutral plane, radial compression (P) axes (i.e., they point toward the load). For concave upward curvature, the predicted stresses in 2D are opposite (radial compression (P) axes above, and radial extension (T) axes below the neutral plane). Compression and extension axes are swapped across a change in curvature because the 2D model is unable to account for the observed tangential orientation of deep T axes (only the radial and vertical dimensions exist), instead predicting vertical T axes. When the tangential dimension is included in our 3D models, the principal stresses and effects across a change curvature are different. In 3D, deep radial compression (P) axes rotate from dominantly horizontal to dominantly vertical as curvature transitions from concave-down to concave-up, and the extension (T) axis is tangential and constant (Figure 8b). Therefore, a key difference between the 2D and 3D predictions is that the former predicts a swap of P and T axes occurs across a change in curvature, while the latter predicts that the only variation is in the dip angle of the radial axis. This is significant to interpreting observations at Hawaii, because the more complete 3D models suggest that we should seek radial P axes with a dip angle that exceeds 45° as evidence of a change in curvature and a coherent Hawaiian lithosphere, and not a transition to radial T axes as suggested by 2D models.

We have shown the dip angles of deep radial P axes are essential to determining whether the lithosphere undergoes a change in curvature but, unfortunately, dominantly vertical P axes were previously discarded due to increased uncertainty in azimuth (Klein, 2016). As a result, the available data set artificially excludes dip angles exceeding 45° , and whether or where a change in curvature occurs is unknown. If we presume that the discarded events are in fact negligible, then the dominantly horizontal and radial P axis solutions are observationally consistent with no change in the sign of curvature based on the 2D model used previously as well as the new 3D results.

That our preferred Model nine exhibits a change in curvature at 50–100 km radius suggests the nonlinear weakening in our models is insufficient to reproduce observations that are consistent with an effectively broken plate. A localized reduction in strength (e.g., μ_f) would be required to reduce the radius at which the change in curvature occurs to <30 km (the observed low-seismicity zone). On the other hand, if discarded dominantly vertical P axes are non-negligible, then reincorporating these events to the data set could show a change in curvature occurs, and the radius at which the change occurs could be used to further constrain lateral variations in strength in future studies.

6. Conclusions

We have compiled the first estimate of seismic strain rate in the lithosphere at the Hawaiian Islands based on 60 years of recorded seismic activity. The magnitude of the 1D vertical seismic strain rate profile is 10^{-16} s^{-1} to 10^{-18} s^{-1} in the upper 35 km of the lithosphere and reduces to a local minimum at the neutral bending plane or ~ 15 km depth. We compute the time-dependent response of the lithosphere to Hawaiian Island building in 3D viscoelastic loading models with nonlinear, laboratory-derived rheology including frictional sliding, low-temperature plasticity, and high-temperature creep. To fit observations of flexure and the seismic strain rate, our viscoelastic loading models indicate that the preferred value of the frictional coefficient at Hawaii is $\mu_f = 0.3 \pm 0.1$. However, the seismic and model strain rates also suggest that significant lateral variations in μ_f may exist such that μ_f is reduced at the load-center where the stress is maximal, most likely due to the effects of dynamic weakening. This new constraint on frictional sliding also improves previous estimates of the degree of weakening required for laboratory-derived low-temperature plasticity to reproduce the observed flexure at the Hawaiian Islands. Low-temperature plasticity published by Idrissi et al. (2016) can be calibrated to lithospheric conditions by reducing the plastic activation energy from 566 to 420 kJ/mol, which is a very modest reduction considering the ± 74 kJ/mol uncertainty associated with this parameter value. Our study thus represents an essential test of whether extrapolating low-temperature plasticity and frictional sliding from laboratory conditions to lithospheric conditions is viable, and demonstrates some modification is required.

The 3D principal stress field from models reproduces the observed radial pattern of P axes below the neutral plane, and tangential T axes. Our results overestimate the dip angle of deep radial P axes, but this disagreement may be artificial because dominantly vertical P axes were previously discarded from the observational study (Klein, 2016). Our 3D models reveal that the dip angle of radial axes is central to understanding curvature, lateral variations in strength and therefore whether the Hawaiian lithosphere is broken or coherent. We suggest the discarded, dominantly vertical P axes should be reconsidered because they may hold the key to discerning whether the lithosphere exhibits a change in curvature. Finally, our study raises an important question on lithospheric deformation and the emergence of plate tectonics, that is, what physical mechanisms and processes cause the effective coefficient of friction to reduce from stable plate interiors to active deformation zones either beneath the Hawaiian Islands or at active plate boundaries? For example, is strain softening sufficient to reproduce lateral variations in the seismic strain rate and the dip angle of P axes at the Island of Hawaii? This indicates an important topic to explore in future laboratory and modeling studies.

Conflict of Interests

The authors declare no competing financial interests.

Data Availability Statement

Codes used to compute the seismic strain rate from magnitude-location data are available for download from doi.org/10.6084/m9.figshare.13151087. Seismic data are openly available for download from the USGS, which hosts the ANSS ComCat (<https://earthquake.usgs.gov/earthquakes/search/>). The numerical viscoelastic loading code and all other materials of this study are uploaded to <https://doi.org/10.6084/m9.figshare.13930448>. Correspondence and requests for materials should be addressed to A. Bellas (ashley.bellas@colorado.edu) or S. J. Zhong (szhong@colorado.edu).

Acknowledgments

The authors are grateful to Dr. John Naliboff and an anonymous reviewer for highly constructive and insightful reviews. This work was supported by NSF grant EAR-1940026 without which the study would not be possible.

References

Behn, M. D., Lin, J., & Zuber, M. T. (2002). Evidence for weak oceanic transform faults. *Geophysical Research Letters*, 29(24), 2207. <https://doi.org/10.1029/2002GL015612>

Bellas, A., Zhong, S., & Watts, A. (2020). Constraints on the rheology of the lithosphere from flexure of the Pacific plate at the Hawaiian Islands. *Geochemistry, Geophysics, Geosystems*, 21, e2019GC008819. <https://doi.org/10.1029/2019GC008819>

Bercovici, D., & Ricard, Y. (2014). Plate tectonics, damage, and inheritance. *Nature*, 508, 513–516.

Billen, M., Cowgill, E., & Buer, E. (2007). Determination of fault friction from reactivation of abyssal-hill faults in subduction zones. *Geology*, 35(9), 819–822. <https://doi.org/10.1130/g23847a.1>

Billen, M. I. (2020). Deep slab seismicity limited by rate of deformation in the transition zone. *Science Advances*, 6, eaaz7692. <https://doi.org/10.1126/sciadv.aaz7692>

Boettcher, M. S., Hirth, G., & Evans, B. (2007). Olivine friction at the base of oceanic seismogenic zones. *Journal of Geophysical Research*, 112, B01205. <https://doi.org/10.1029/2006JB004301>

Bull, J. M., & Scrutton, R. A. (1990). Fault reactivation in the central Indian Ocean and the rheology of oceanic lithosphere. *Nature*, 344, 855–858. <https://doi.org/10.1038/344855a0>

Byerlee, J. (1978). Friction of rocks. *Pure and Applied Geophysics*, 116, 615–626. https://doi.org/10.1007/978-3-0348-7182-2_4

Chernak, L. J., & Hirth, G. (2010). Deformation of antigorite serpentinite at high temperature and pressure. *Earth and Planetary Science Letters*, 296, 23–33. <https://doi.org/10.1016/j.epsl.2010.04.035>

Christensen, N. I. (1966). Elasticity of ultrabasic rocks. *Journal of Geophysical Research*, 71(24), 5921–5931. <https://doi.org/10.1029/jz071i024p05921>

Colletini, C. (2011). The mechanical paradox of low-angle normal faults: Current understanding and open questions. *Tectonophysics*, 510, 253–268. <https://doi.org/10.1016/j.tecto.2011.07.015>

Craig, T. J., Copley, A., & Middleton, T. A. (2014). Constraining fault friction in oceanic lithosphere using the dip angles of newly-formed faults at outer rises. *Earth and Planetary Science Letters*, 392, 94–99. <https://doi.org/10.1016/j.epsl.2014.02.024>

England, P. (2018). On shear stresses, temperatures, and the maximum magnitudes of earthquakes at convergent plate boundaries. *Journal of Geophysical Research: Solid Earth*, 123, 7165–7202.

England, P., & Molnar, P. (1997). Active deformation of Asia: from kinematics to dynamics. *Science*, 278, 647–650. <https://doi.org/10.1126/science.278.5338.647>

Escartin, J., Hirth, G., & Evans, B. (1997). Nondilatant brittle deformation of serpentinites: Implications for Mohr-Coulomb theory and the strength of faults. *Journal of Geophysical Research*, 102(B2), 2897–2913. <https://doi.org/10.1029/96jb02792>

Freed, A. M., Herring, T., & Bürgmann, R. (2010). Steady-state laboratory flow laws alone fail to explain postseismic observations. *Earth and Planetary Science Letters*, 300, 1–10. <https://doi.org/10.1016/j.epsl.2010.10.005>

Gao, X., & Wang, K. (2014). Strength of stick-slip and creeping subduction megathrusts from heat flow observations. *Science*, 345, 1038–1041. <https://doi.org/10.1126/science.1255487>

Goetze, C., & Evans, B. (1979). Stress and temperature in the bending lithosphere as constrained by experimental rock mechanics. *Geophysical Journal International*, 59, 463–478. <https://doi.org/10.1111/j.1365-246x.1979.tb02567.x>

Gordon, R. G. (2000). Diffuse oceanic plate boundaries: Strain-rates, vertically averaged rheology and comparisons with narrow plate boundaries and stable plate interiors. In M. A. Richards, R. G. Gordon, & R. D. van der Hilst, (Eds.), *The History and Dynamics of global plate motions, Geophysical Monograph Series* (pp. 143–159). Washington, DC: American Geophysical Union.

Guest, I., Ito, G., Garcia, M. O., & Hellebrand, E. (2020). Extensive magmatic heating of the lithosphere beneath the Hawaiian Islands inferred from Salt Lake Crater Mantle xenoliths. *Geochemistry, Geophysics, Geosystems*, 21(12), e2020GC009359. <https://doi.org/10.1029/2020GC009359>

Hansen, L. N., David, E. C., Brantut, N., & Wallis, D. (2020). Insight into the microphysics of antigorite deformation from spherical nanoindentation. *Philosophical Transactions of the Royal Society A*, 378, 20190197. <https://doi.org/10.1098/rsta.2019.0197>

Hansen, L. N., Kumamoto, K. M., Thom, C. A., Wallis, D., Durham, W. B., & Goldsby, D. L., et al. (2019). Low-Temperature Plasticity in Olivine: Grain Size, Strain Hardening, and the Strength of the Lithosphere. *Journal of Geophysical Research: Solid Earth*, 124, 5427–5449. <https://doi.org/10.1029/2018JB016736>

Hirth, G., & Kohlstedt, D. L. (2003). Rheology of the upper mantle and the mantle wedge: A view from the experimentalists. In J. Eiler, (Ed.), *Inside the subduction factory, Geophysical Monograph Series* (pp. 83–105). Washington, DC: American Geophysical Union.

Holt, W. E., Li, M., & Haines, A. J. (1995). Earthquake strain rates and instantaneous relative motions within central and eastern Asia. *Geophysical Journal International*, 122, 569–593. <https://doi.org/10.1111/j.1365-246x.1995.tb07014.x>

Hu, Y., & Wang, K. (2012). Spherical-earth finite element model of short-term postseismic deformation following the 2004 Sumatra earthquake. *Journal of Geophysical Research*, 117, B05404. <https://doi.org/10.1029/2012JB009153>

Huismans, R. S., & Beaumont, C. (2003). Symmetric and asymmetric lithospheric extension: Relative effects of frictional-plastic and viscous strain softening. *Journal of Geophysical Research*, 108, 2496. <https://doi.org/10.1029/2002JB002026>

Hunter, J., & Watts, A. B. (2016). Gravity anomalies, flexure and mantle rheology seaward of circum-Pacific trenches. *Geophysical Journal International*, 207, 288–316. <https://doi.org/10.1093/gji/ggw275>

Idrissi, H., Bollinger, C., Bolioli, F., Schryvers, D., & Cordier, P. (2016). Low-temperature plasticity of olivine revisited with in situ TEM nanomechanical testing. *Science Advances*, 2(3), e1501671. <https://doi.org/10.1126/sciadv.1501671>

Jackson, J., & McKenzie, D. (1988). The relationship between plate motions and seismic moment tensors, and the rates of active deformation in the Mediterranean and Middle East. *Geophysical Journal International*, 93, 45–73. <https://doi.org/10.1111/j.1365-246x.1988.tb01387.x>

Jain, C., Korenaga, J., & Karato, S. I. (2017). On the yield strength of oceanic lithosphere. *Geophysical Research Letters*, 44, 9716–9722. <https://doi.org/10.1002/2017gl075043>

Karato, S., & Barbot, S. (2018). Dynamics of fault motion and the origin of contrasting tectonic style between Earth and Venus. *Scientific Reports*, 8(1184), 1–11. <https://doi.org/10.1038/s41598-018-30174-6>

Katayama, I., & Karato, S.-I. (2008). Low-temperature, high-stress deformation of olivine under water-saturated conditions. *Physics of the Earth and Planetary Interiors*, 168, 125–133. <https://doi.org/10.1016/j.pepi.2008.05.019>

Klein, F. W. (2016). Lithospheric flexure under the Hawaiian volcanic load: Internal stresses and a broken plate revealed by earthquakes. *Journal of Geophysical Research: Solid Earth*, 121, 2400–2428. <https://doi.org/10.1002/2015JB012746>

Kostrov, V. V., & Goodspeed, F. (1974). Seismic moment and energy of earthquakes and seismic flow of rock. *Izv. Earth Physics*, 1, 23–40.

- Kumamoto, K., Thom, C. A., Wallis, D., Hansen, L. N., Armstrong, D. E. J., & Warren, J. M. (2017). Size effects resolve discrepancies in 40 years of work on low-temperature plasticity in olivine. *Science Advances*, 3(e1701338), 1–6.
- Laske, G., Markee, A., Orcutt, J. A., Wolfe, C. J., Collins, J. A., Solomon, S. C., et al. (2011). Asymmetric shallow mantle structure beneath the Hawaiian Swell—evidence from Rayleigh waves recorded by the PLUME network. *Geophysical Journal International*, 187, 1725–1742. <https://doi.org/10.1111/j.1365-246x.2011.05238.x>
- Masson, F., Chéry, J., Hatzfeld, D., Martinod, J., Vernant, P., Tavakoli, F., & Ghafory-Ashtiani, M. (2005). Seismic versus aseismic deformation in Iran inferred from earthquakes and geodetic data. *Geophysical Journal International*, 160, 217–226.
- McGovern, P. J. (2007). Flexural stresses beneath Hawaii: Implications for the October 15, 2006, earthquakes and magma ascent. *Geophysical Research Letters*, 34, L23305. <https://doi.org/10.1029/2007GL031305>
- Mei, S., Suzuki, A. M., Kohlstedt, D. L., Dixon, N. A., & Durham, W. B. (2010). Experimental constraints on the strength of the lithospheric mantle. *Journal of Geophysical Research*, 115, B08204. <https://doi.org/10.1029/2009JB006873>
- Meyer, S. E., Kaus, B. J. P., & Passchier, C. (2017). Development of branching brittle and ductile shear zones: A numerical study. *Geochemistry, Geophysics, Geosystems*, 18, 2054–2075. <https://doi.org/10.1002/2016GC006793>
- Mitrovica, J. X., & Forte, A. M. (1997). Radial profile of mantle viscosity: Results from the joint inversion of convection and postglacial rebound observables. *Journal of Geophysical Research*, 102, 2751–2769. <https://doi.org/10.1029/96jb03175>
- Molnar, P. (2020). The brittle-plastic transition, earthquakes, temperatures, and strain rates. *Journal of Geophysical Research: Solid Earth*, 125, e2019JB019335. <https://doi.org/10.1029/2019jb019335>
- Moore, J. G., & Clague, D. A. (1992). Volcano growth and evolution of the island of Hawaii. *The Geological Society of America Bulletin*, 104, 1471–1484. [https://doi.org/10.1130/0016-7606\(1992\)104<1471:vgaet>2.3.co;2](https://doi.org/10.1130/0016-7606(1992)104<1471:vgaet>2.3.co;2)
- Moresi, L., & Solomatov, V. (1998). Mantle convection with a brittle lithosphere: Thoughts on the global tectonic styles of the Earth and Venus. *Geophysical Journal International*, 133, 669–682. <https://doi.org/10.1046/j.1365-246x.1998.00521.x>
- Naliboff, J. B., Glerum, A., Brune, S., Péron-Pinvidic, G., & Wrona, T. (2020). Development of 3-D rift heterogeneity through fault network evolution. *Geophysical Research Letters*, 47, e2019GL086611. <https://doi.org/10.1029/2019gl086611>
- Pleus, A., Ito, G., Wessel, P., & Frazer, L. N. (2020). Rheology and thermal structure of the lithosphere beneath the Hawaiian Ridge inferred from gravity data and models of plate flexure. *Geophysical Journal International*, ggaal155. <https://doi.org/10.1093/gji/ggaal155>
- Podolefsky, N. S., Zhong, S., & McNamara, A. K. (2004). The anisotropic and rheological structure of the oceanic upper mantle from a simple model of plate shear. *Geophysical Journal International*, 158, 287–296. <https://doi.org/10.1111/j.1365-246x.2004.02250.x>
- Pritchard, M. E., Rubin, A. M., & Wolfe, C. J. (2007). Do flexural stresses explain the mantle fault zone beneath Kilauea volcano? *Geophysical Journal International*, 168, 419–430. <https://doi.org/10.1111/j.1365-246x.2006.03169.x>
- Raterron, P., Wu, Y., Weidner, D. J., & Chen, J. (2004). Low-temperature olivine rheology at high pressure. *Physics of the Earth and Planetary Interiors*, 145, 149–159. <https://doi.org/10.1016/j.pepi.2004.03.007>
- Reuber, G. S., Holbach, L., Popov, A. A., Hanke, M., & Kaus, B. J. P. (2020). Inferring rheology and geometry of subsurface structures by adjoint-based inversion of principal stress directions. *Geophysical Journal International*, 223(2), 851–861. <https://doi.org/10.1093/gji/ggaa344>
- Ribe, N. M., & Christensen, U. R. (1994). Three-dimensional modeling of plume-lithosphere interaction. *Journal of Geophysical Research*, 99, 669–682. <https://doi.org/10.1029/93jb02386>
- Ross, S. L., Michael, A. J., Klein, F. W., Kirby, S. L., & Hardebeck, J. L. (2007). *Insights into the 2006 Kiholo, Hawaii, earthquake and Pacific Plate flexure from double-difference relocations and stress inversions (abstract)*. 2007 SSA annual meeting, Hawaii: Kona.
- Shor, G. G., & Pollard, D. D. (1964). Mohole site selection studies north of Maui. *Journal of Geophysical Research*, 69, 1627–1637. <https://doi.org/10.1029/jz069i008p01627>
- Swanson, D., Duffield, W. A., & Fiske, R. (1976). Displacement of the south flank of Kilauea volcano: The result of forceful intrusion of magma into the rift zones. *Geological survey professional paper*, 963. <https://doi.org/10.3133/pp963>
- Thatcher, W., & Hill, D. P. (1995). A simple model for the fault-generated morphology of slow-spreading mid-oceanic ridges. *Journal of Geophysical Research*, 100(B1), 561–570. <https://doi.org/10.1029/94jb02593>
- Vanhunen, J., Zhong, S., Shapiro, N., & Ritzwoller, M. (2005). New evidence for dislocation creep from 3-D geodynamic modeling of the Pacific upper mantle structure. *Earth and Planetary Science Letters*, 238, 146–155. <https://doi.org/10.1016/j.epsl.2005.07.006>
- von Herzen, R. P., Cordery, M. J., Detrick, R. S., & Fang, C. (1989). Heat flow and the thermal origin of hot spot swells: The Hawaiian swell revisited. *Journal of Geophysical Research*, 94, 13783–13799. <https://doi.org/10.1029/jb094ib10p13783>
- Watts, A. B., & ten Brink, U. S. (1989). Crustal structure, flexure and subsidence history of the Hawaiian Islands. *Journal of Geophysical Research*, 94(10), 473–410. <https://doi.org/10.1029/jb094ib08p10473>
- Watts, A. B., & Zhong, S. (2000). Observations of flexure and the rheology of oceanic lithosphere. *Geophysical Journal International*, 142, 855–875. <https://doi.org/10.1046/j.1365-246x.2000.00189.x>
- Wessel, P. (1993). A reexamination of the flexural deformation beneath the Hawaiian Islands. *Journal of Geophysical Research*, 98(12), 17719–17721. <https://doi.org/10.1029/93jb00523>
- Wiens, D. A., & Stein, S. (1983). Age dependence of oceanic intraplate seismicity and implications for lithospheric evolution. *Journal of Geophysical Research*, 88, 6455–6468. <https://doi.org/10.1029/jb088ib08p06455>
- Wolfe, C. J., Okubo, P. G., & Shearer, P. M. (2003). Mantle fault zone beneath Kilauea volcano, Hawaii. *Science*, 300, 478–480.
- Wu, P. (1992). Deformation of an incompressible viscoelastic flat earth with powerlaw creep: A finite element approach. *Geophysical Journal International*, 108(1), 35–51. <https://doi.org/10.1111/j.1365-246x.1992.tb00837.x>
- Young, J. B., Presgrave, B. W., Aichele, H., Wiens, D. A., & Flinn, E. A. (1996). The Flinn-Engdahl Regionalization Scheme: The 1995 revision. *Physics of the Earth and Planetary Interiors*, 96, 223–297. [https://doi.org/10.1016/0031-9201\(96\)03141-x](https://doi.org/10.1016/0031-9201(96)03141-x)
- Zhong, S., & Watts, A. B. (2013). Lithospheric deformation induced by loading of the Hawaiian Islands and its implications for mantle rheology. *Journal of Geophysical Research: Solid Earth*, 118, 6025–6048. <https://doi.org/10.1002/2013JB010408>
- Zhong, S. J., Paulson, A., & Wahr, J. (2003). Three-dimensional finite-element modelling of Earth's viscoelastic deformation: Effects of lateral variations in lithospheric thickness. *Geophys. J. Int.*, 155, 679–695.
- Zoback, M. D., & Townend, J. (2001). Implications of hydrostatic pore pressures and high crustal strength for the deformation of intraplate lithosphere. *Tectonophysics*, 336, 19–30. [https://doi.org/10.1016/s0040-1951\(01\)00091-9](https://doi.org/10.1016/s0040-1951(01)00091-9)
- Zucca, J. J., Hill, D. P., & Kovach, R. L. (1982). Crustal structure of Mauna Loa Volcano, Hawaii, from seismic refraction and gravity data. *Bulletin of the Seismological Society of America*, 72, 1535–1550.